

# Automated Skin Lesion Diagnosis and Classification Using Learning Algorithms

A. Soujanya<sup>1,\*</sup> and N. Nandhagopal<sup>2</sup>

<sup>1</sup>Department of Information and Communication Engineering, Anna University, Chennai, 600025, Tamil Nadu, India

<sup>2</sup>Department of Electronics and Communication Engineering, Excel Engineering College, Namakkal, 638052, Tamil Nadu, India

\*Corresponding Author: A. Soujanya. Email: annaramsoujanya05@gmail.com

Received: 09 December 2021; Accepted: 10 January 2022

**Abstract:** Due to the rising occurrence of skin cancer and inadequate clinical expertise, it is needed to design Artificial Intelligence (AI) based tools to diagnose skin cancer at an earlier stage. Since massive skin lesion datasets have existed in the literature, the AI-based Deep Learning (DL) models find useful to differentiate benign and malignant skin lesions using dermoscopic images. This study develops an Automated Seeded Growing Segmentation with Optimal EfficientNet (ARGS-OEN) technique for skin lesion segmentation and classification. The proposed ASRGS-OEN technique involves the design of an optimal EfficientNet model in which the hyper-parameter tuning process takes place using the Flower Pollination Algorithm (FPA). In addition, Multiwheel Attention Memory Network Encoder (MWAMNE) based classification technique is employed for identifying the appropriate class labels of the dermoscopic images. A comprehensive simulation analysis of the ASRGS-OEN technique takes place and the results are inspected under several dimensions. The simulation results highlighted the supremacy of the ASRGS-OEN technique on the applied dermoscopic images compared to the recently developed approaches.

**Keywords:** Computer aided diagnosis; deep learning; image segmentation; skin lesion diagnosis; dermoscopic images; medical image processing

## 1 Introduction

According to the Skin Cancer Foundation, the global incidence of skin cancer is growing [1]. Melanoma cases are predicted to reach 192,310 in the United States in 2019. However, non-melanocytic skin malignancies such as Squamous Cell Carcinoma (SCC) and Basal Cell Carcinoma (BCC) are more prevalent [2,3]. Early diagnosis of the skin lesion is critical for optimising outcomes and is associated with a 99 percent overall survival rate (OS). However, when illnesses spread beyond the skin, survival rates might be low [4]. A dermatologist examines a patient visually using polarised light magnification using dermoscopy in current clinical practise. Medicinal diagnoses are frequently made on the basis of ethnic origin, patient history, sun exposure, and social habits. Concerning lesions are sent to the laboratory, biopsied in the office, evaluated on representative glass slides, and processed as permanent paraffin sections by pathologists for diagnosis [5]. A computer-aided diagnostics (CAD) system powered by artificial intelligence is on the verge of changing health care and medicine, notably in the field of



This work is licensed under a Creative Commons Attribution 4.0 International License, which permits unrestricted use, distribution, and reproduction in any medium, provided the original work is properly cited.

medicinal imaging. Medical imaging procedures such as computed tomography (CT), magnetic resonance imaging (MRI), and ultrasound are widely used in clinical practise [6]. In numerous types of research, AI systems outperform/equal physician performance in diagnosing disease using medical imaging. Recent advances in deep learning have enabled the detection of anomalies such as brain tumours, breast cancer, esophageal cancer, skin lesions, foot ulcers, and lung cancer across a variety of image modalities used in medical imaging [7]. Convolutional Neural Networks (CNNs) have been identified as an invaluable tool for biomedical image classifiers and have been proposed as a tool for medical diagnosis in the histology, radiology, dermatology, and ophthalmology disciplines in the last few years [8]. The rapid growth of CNN and other deep learning algorithms has necessitated that non-experts get familiar with and grasp this sophisticated instrument. A comprehensive assessment of introductory publications providing a fundamental overview of CNN applications and principles exists [9]. Banerjee et al. [10] offer a DL-based 'You Only Look Once' (YOLO) approach that is based on Deep Convolutional Neural Network (DCNN) applications to diagnose melanoma using digital and skin lesion images and produces more precise and faster output than typical CNN methods. In terms of the location of detected items within the cell, these networks predict the bounding box for both the class confidence score and the recognised object. However, this study distinguishes itself through the incorporation of several resourceful models, including two-stage segmentation performed with the integration of the graph concept via L-type fuzzy numbers and the minimum spanning tree concept, as well as numerical extractions of the cancer area's actually infected region during the feature extraction processes. Khan et al. [11] employ a (IMFO) algorithm to determine the most discriminating feature. The generated feature is then combined with classifiers based on Multiset Maximum Correlation Analysis (MMCA) and Kernel Extreme Learning Machine (KELM).

Sikkandar et al. [12] integrate Adaptive Neuro-Fuzzy Classifier (ANFC) and GrabCut algorithms to offer novel segmentation-based classification models for skin lesion diagnosis. Segmentation, preprocessing, classification, and feature extraction are the four primary phases of the described model. To begin, preprocessing can be accomplished using inpainting and Top hat filter approaches. Following that, the pre-processed image is segmented using the Grabcut algorithms. Then, the feature extraction is performed using the Inception module, which is based on deep learning. Finally, an ANFC model is used to classify the skin lesion photos. Srinivasu et al. [13] demonstrated an automated technique for identifying skin illnesses using the Distributed Learning (DL)-based MobileNet V2 and Long Short-Term Memory (LSTM). The MobileNet V2 technique has been demonstrated to be effective, with enhanced performance on lightweight compute devices. The rise of illness progression is quantified using a grey level co-occurrence matrix.

This work develops an ARGS-OEN technique for segmenting and classifying skin lesions. The suggested ASRGS-OEN technique entails creating an ideal EfficientNet model and tweaking the hyperparameters using the FPA. Additionally, a classification model based on MWAMNE is used. The ASRGS-OEN technique is subjected to a thorough simulation examination, with the findings analysed across a variety of dimensions.

## 2 The Proposed Model

In this study, a novel ASRGS-OEN technique is developed for diagnosing and classifying the distinct stages of skin diseases. The proposed ASRGS-OEN technique incorporates different sub-processes namely preprocessing, SRG based segmentation, EfficientNet based feature extraction, and MWAMNE based classification. Fig. 1 demonstrates the overall process of the ASRGS-OEN model. The working of these modules is offered in the subsequent sections.

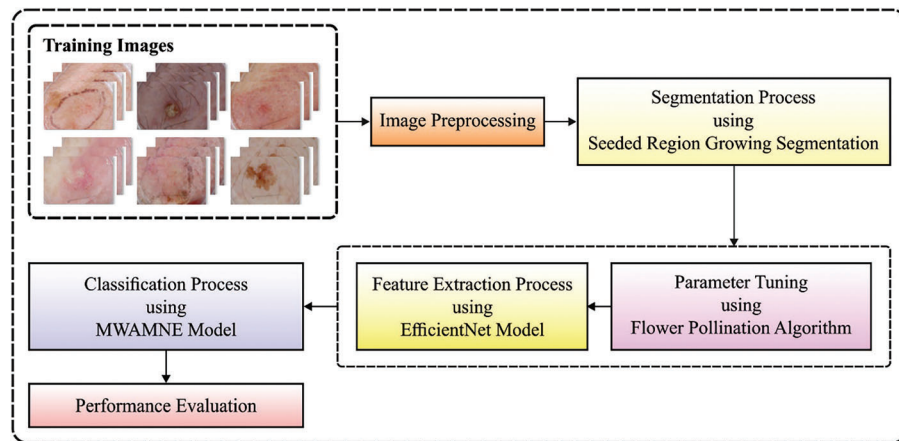


**Figure 1:** Overall block diagram of ASRGS-OEN model

## 2.1 Preprocessing

The image pre-processed manner contains identifying of lesion place under the image as well as hair removals. Primarily, the images have been resized as to uniform size, and class label procedure occurs. This data composes values of in-between coordinate points such as width ( $w$ ) and height ( $h$ ) of bounding boxes in which class description of objects requires that defined. Also, the hair removals procedure happens on the dermoscopic image with utilize of DullRazor [14] manner for precisely detecting as well as removing hairs. For achieving this, initially, the place of hair has been identified utilizing the grayscale morphological closing functions. Afterward, the hair place has been making sure that defining the length as well as thickness of the defined shape, and pixel obtain replaced with utilize of bilinear interpolation manner.

## 2.2 Image Segmentation Using SRG Technique

At this stage, the preprocessed image is applied to the SRG technique to determine the affected lesion regions in the image. The Seeded Region Growing (SRG) technique is an effective image segmentation method for medicinal images since it can be fast and robust. In these techniques, the seed point is automatically selected and the rest of the neighbor pixels are related based on automatically chosen threshold  $T$ . It has a variety of applications in different areas: In the medicinal image segmentation, it is applied to skin lesion areas. It employs a data structure known as Sequentially Sorted List (SSL). The SSL might be a connected list i.e., well-ordered according to certain features. Once a novel pixel is connected with the region, it should be maintained as per the pixel value of the ordered attribute. The SRG is the same as flood fill and Breadth-First Search (BFS) models [15]. Region growing image segmentation is practiced considerably while the region of interest and the background have overspreading pixels intensity. The steps of the original SRG are given below:

Step 1: The first seed point is fixed as  $P_1, P_2, \dots, P_n$ , which is segmented to  $C_1, C_2, \dots, C_n$ .

Step 2: When  $|P_i \text{ neighbor pixel value}| < \text{threshold}$ , the neighboring points are categorized to  $C_i$ , whereas  $i = 1, 2, \dots, n$ .

Step 3: The novel boundary of  $C_i$  is estimated as novel seed point i.e.,  $P_i$ s. The mean pixel intensity value of segments  $C_i$  must be recomputed, correspondingly.

Step 4: Continue Steps 2 & 3 till the points where each pixel in an image species to one of the segments.

### 2.3 Feature Extraction Using Optimal EfficientNet Model

Next to image segmentation, the optimal subset of feature vectors is derived by the use of EfficientNet model. The EfficientNet technique is presented by Tan that is attain an appropriate outcome on the increase of depth, width, and resolution of networks, and next attain optimum technique efficiency. Initial, it can determine a CNNs as function:  $Y_i = F_i(X_i)$ , where  $F_i$  implies the operators (op),  $Y_i$  refers the tensor of outputs,  $X_i$  signify the input tensor of shape  $\langle H_i, W_i, C_i \rangle$ , where  $H_i$ ,  $W_i$ , and  $C_i$  refers the height, width, and amount of channels of input images. The CNN Net is explained as a series of collected layers:  $Net = F_k \odot \dots \odot F_2 \odot F_1(X_1) = \odot_{j=1\dots k} F_j(X_1)$ . During the actual application procedure, the CNN layer has been generally implemented in several stages, and all stages utilize a similar network framework. So, it can be determined as:

$$Net = \odot_{i=1\dots s} F_i^{L_i}(X_{\langle H_i, W_i, C_i \rangle}) \quad (1)$$

where  $F_i^{L_i}$  implies the layers  $F_i$  has been repeated  $L_i$  times in a stage  $i$ ,  $\langle H_i, W_i, C_i \rangle$  demonstrates the height, width, and the amount of channels of an input tensor  $X$  of the layer  $i$ . Second, the ordered CNN structures mostly effort on determining a better layer structure  $F_i$ . But, dependent upon existing  $F_i$  baseline network framework, technique scaling mostly tries to increase the network length ( $L_i$ ), width ( $C_i$ ), and/or resolution ( $H_i, W_i$ ). In the meantime, model scaling overcome the strategy issue to a novel resource constraint by fitting  $F_i$ , and it explores distinct  $L_i, C_i, H_i, W_i$ , to all layers because of their sample design space [16]. The target has to considerably enhance the accuracy of technique in some provided resource constraints, and that is considered as subsequent optimized issue:

$$\max_{d,w,r} Accuracy(Net(d, w, r))$$

$$s. t. Net(d, w, r) = \odot_{j=1\dots k} \hat{F}_i^{d \cdot \hat{L}_i}(X_{\langle r \cdot \hat{H}_i, r \cdot \hat{W}_i, w \cdot \hat{C}_i \rangle})$$

$$Memory(Net) \leq target\_memory$$

$$FLOPS(Net) \leq target\_flops \quad (2)$$

where  $w, d, r$  implies the coefficients are utilized to scaling network width, depth, and resolution;  $\hat{F}_i, \hat{L}_i, \hat{H}_i, \hat{W}_i, \hat{C}_i$ , demonstrates the existing parameters under the baseline networks. Third, a novel compound scaling manner with compound coefficients  $\phi$  has been utilized for uniformly expanding network depth, width, and resolution under a stated manner:

$$depth: d = \alpha^\phi$$

$$width: w = \beta^\phi$$

$$resolution: r = \gamma^\phi$$

$$s. t. \alpha \cdot \beta^2 \cdot \gamma^2 \approx 2$$

$$\alpha \geq 1, \beta \geq 1, \gamma \geq 1 \quad (3)$$

where  $\alpha, \beta, \gamma$  implies the constants. Amongst them,  $\phi$  has been identified value which defines several more resources are valid to model increasing, but  $\alpha, \beta, \gamma$  define that distributing these extra resources for network width, depth, and resolution correspondingly. Also, it can be detailed connection amongst the FLOPS of

regular convolutional op and d,  $w^2$ ,  $r^2$ . As the convolutional ops frequently controlling the computation cost from CNN, increasing a CNN by utilizing Eq. (3) is around improve entire FLOPS by  $(\alpha \cdot \beta^2 \cdot \gamma^2)^\phi$ . Eventually, the model scaling doesn't alter layer operator  $F_i$  in the existing baseline network, therefore, it can be also serious to have optimum baseline networks.

Since hyper-parameters play a vital role in classification efficiency, they are optimally adjusted by the use of FPA. The abiotic pollination, cross-pollination, self-pollination, and biotic pollination approaches have been determined in domain optimizing as well as embedding under the FPA. This pollination procedure contains an order of difficult methods during plant-making approaches. The flower and their pollen gametes procedure a solution of the optimized issue. Conversely, the local pollination in a restricted region of unique flower occurs in shading with wind or water. Global pollination happens with probabilities that are known as switch probability. When this step has been eliminated, local pollination changes it. During the FPA technique 4 principles are followed: (i) live pollination and cross-pollination have been regarded as global pollination and the carry or pollen pollinator transfers in the direction which follows levy flight; (ii) abiotic and self-pollination were assumed as local pollination; (iii) pollinators containing insects are made flower constancies. The flower constancy has been production probabilities which are proportional to the comparison of 2 difficult flowers, and (iv) the interaction of global as well as local pollination are managed with switch probabilities.

The 1<sup>st</sup> and 3<sup>rd</sup> principles are written as:

$$x_i^{t+1} = x_i^t + \gamma \times L(\lambda) \times (g_* - x_i^t) \quad (4)$$

where  $x_i^t$  represents the pollen/solution vectors at iteration t;  $g_*$  implies the present optimum solutions amongst every present generation solution;  $\gamma$  refers the scale factor to control step sizes, and L signifies the strength of pollinations that has been step size compared with Levy Distribution (LD) [17]. The levy flight has been a bunch of arbitrary procedures in which the length of all jumps follows the levy probability distribution function and is infinite difference. Subsequent, L to an LD was provided as:

$$L \sim \frac{\lambda \times \Gamma(\lambda) \times \sin \frac{\pi\lambda}{2}}{\pi} \times \frac{1}{S^{1+\lambda}} S \gg S_0 0, \quad (5)$$

where  $\Gamma(\lambda)$  represents the typical gamma function.

For local pollination, the 2<sup>nd</sup> and 3<sup>rd</sup> principles are provided as:

$$x_i^{t+1} = x_i^t + \epsilon(x_j^t - x_k^t) \quad (6)$$

where  $x_j^t$  and  $x_k^t$  demonstrates 2 pollens in distinct flowers of similar plants. Mathematically, when  $x_j^t$  and  $x_k^t$  come in the similar species or chosen in the similar population, this develops a local arbitrary walk when  $\epsilon$  is a uniform distribution from 0 and 1. Fig. 2 showcases the flowchart of FPA. The size of the population of solutions(n), the scale factor to control step size ( $\gamma$ ), the LD parameters [ $L(\lambda)$ ], and the switch probabilities (P) have been predefined parameters during the FPA. Defining the optimum parameters of FPA has been time-consuming effort and requires running the technique several times. It must be noticeable the optimum parameters of this technique to one issue are distinct in individuals of another issue. Assuming the mixture of parameters has been suitable technique to define the appropriate values of technique parameters. This technique is completed too many times to one mixture of parameters, and the same procedure is frequent to another mixture of parameters. Eventually, the outcomes to distinct groups of parameters are related and an optimum value is defined.

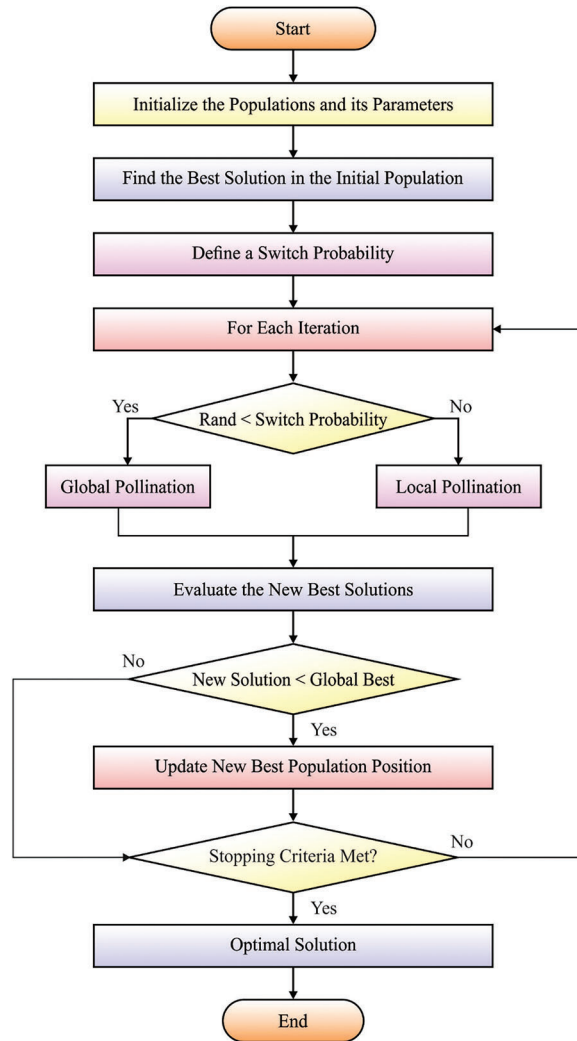


**Figure 2:** Flowchart of FPA

#### 2.4 Image Classification Using MWAMNE Technique

At the last stage, the feature vectors are passed into the MWAMNE technique to allot the proper class labels. Assumed an image  $f$ , its class is  $c$ , represented as  $f_c$  in this work. Firstly, input the images to the benchmark LSTM model and later utilize the LSTM method for calculating the vector of an image as  $V_{f_c} \in \mathbb{R}^d$  can be expressed by

$$V_{f_c} = \text{LSTM}^f(f_c). \quad (7)$$

where each problem shares the encoder  $\text{LSTM}^f$ . This study proposes a network model with many rounds of attention mechanism. Therefore, it allows more precise class identification  $f_c$ . The vector  $V_{f_c}$  illustration for the class detection problems  $f_c$  and the 2 memory banks  $M^I$  &  $M^H$  are related. The problem  $V_{f_c}$  is initially projected to the historical medicinal type memory  $M^H$  by the succeeding equation for retrieving the category fact related to the category detection question  $f_c$ :

$$u_0 = V_{f_c}, \quad (8)$$

$$s_j = u_{j-1} \cdot m_j^H, j = 1, \dots, r, \tag{9}$$

$$u_{j-1} = u_{j-1} + \sum_{i=0}^{c-1} \alpha_i m_i, \alpha_i = \exp(s_i) / \sum_{i=0}^{c-1} \exp(s_i), \tag{10}$$

In the equation,  $r$  stands for the attention mechanism round.  $s_j$  is a measure of similarities among  $u_{j-1}$  &  $m_j^H$ . The  $u_{j-1}$  result is estimated every by the projection issue for categorizing memory [18]. This technique processes the results as the newest expression of the problem  $f_c$  implementing the category. The NN model is later utilized for continually projecting it to the visual fact memory for retrieving the computational correlated visual category fact can be expressed by:

$$h = \tanh(W_{f,h} M^I \oplus (W_u u_{j-1} + b_h)), \tag{11}$$

$$p^I = \text{softmax}(W_p h + b_p), \tag{12}$$

$$u_j = u_{j-1} + \sum_{i=0}^{196} p_i^I m_i^I, \tag{13}$$

In the equation,  $W_{i,h}$ ,  $W_u \in \mathbb{R}^{k \times d}$ , &  $b_h \in \mathbb{R}^k$  mark the addition among the vector and matrix.  $h$  represents the output of the SLNN attained by the prior results achieved by the non-linear hyperbolic tangent function.  $W_p \in \mathbb{R}^{k \times d}$  &  $p^I \in \mathbb{R}^{196}$  represents the projection likelihood values (viz., relation) among every picture region and  $u_{j-1}$ . The output  $u_j$  can be attained by projecting the visual memory.

### 3 Performance Validation

This section investigates the performance of the ASRGS-OEN technique on the applied ISIC dataset [19]. It comprises dermoscopic images of different class labels like Angioma (0), Nevus (1), Lentigo NOS (2), Solar Lentigo (3), Melanoma (4), Seborrheic Keratosis (5), and Basal Cell Carcinoma (6). The confusion matrix of the ASRGS-OEN technique takes place on the applied dataset under the training dataset in Fig. 3. The figure has shown that the ASRGS-OEN technique has categorized 16 images under Angioma class, 41 images in Nevus, 40 images in Lentigo NOS, 62 images in Solar Lentigo, 49 images in Melanoma, 51 images in Seborrheic Keratosis, and 33 images in BCC.

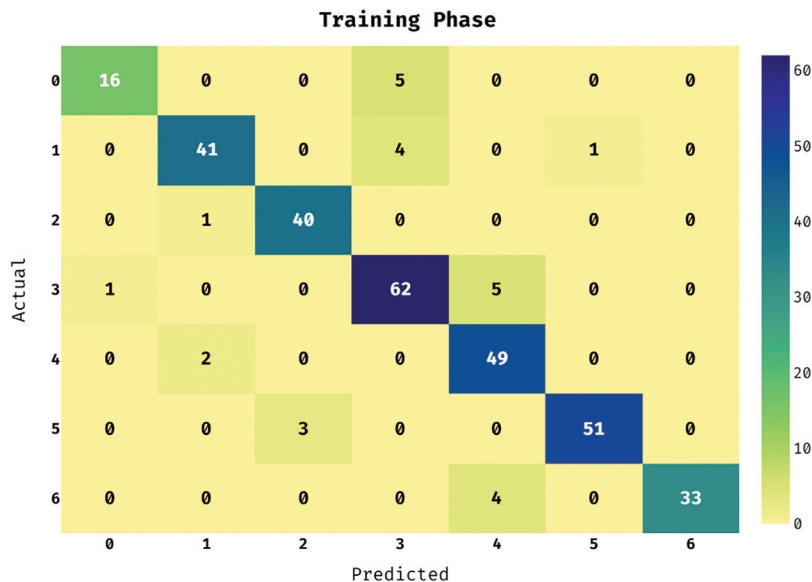
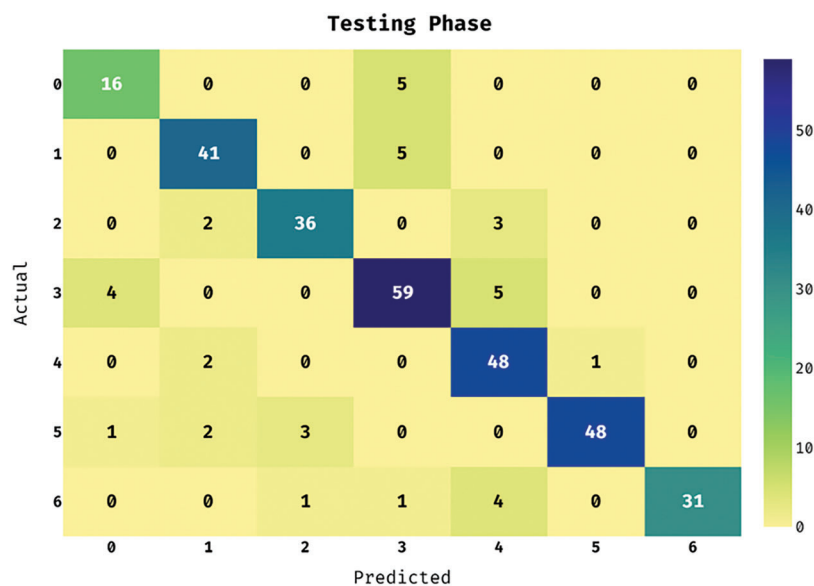


Figure 3: Confusion matrix analysis of under training phase

The confusion matrix of the ASRGS-OEN method takes place on the applied dataset in the testing dataset in Fig. 4. The figure showcased that the ASRGS-OEN approach has categorized 16 images in Angioma class, 41 images in Nevus, 36 images in Lentigo NOS, 59 images under Solar Lentigo, 48 images in Melanoma, 48 images under Seborrheic Keratosis, and 31 images in BCC.



**Figure 4:** Confusion matrix analysis of under testing phase

Tab. 1 offers the classification results analysis of the ASRGS-OEN approach on the applied training and testing dataset. The results have shown that the ASRGS-OEN technique has accomplished effective outcomes under both cases.

**Table 1:** Results analysis of proposed model on training and testing phase

Training phase					
Classes	Accuracy	Sensitivity	Specificity	Precision	F-Score
0	0.9811	0.7619	0.9966	0.9412	0.8421
1	0.9748	0.8913	0.9890	0.9318	0.9111
2	0.9874	0.9756	0.9892	0.9302	0.9524
3	0.9528	0.9118	0.9640	0.8732	0.8921
4	0.9654	0.9608	0.9663	0.8448	0.8991
5	0.9874	0.9444	0.9962	0.9808	0.9623
6	0.9874	0.8919	1.0000	1.0000	0.9429
Average	0.9766	0.9054	0.9859	0.9289	0.9146
Testing Phase					
Classes	Accuracy	Sensitivity	Specificity	Precision	F-Score
0	0.9686	0.7619	0.9832	0.7619	0.7619
1	0.9654	0.8913	0.9779	0.8723	0.8817
2	0.9717	0.8780	0.9856	0.9000	0.8889

(Continued)

**Table 1 (continued)**

Training phase					
Classes	Accuracy	Sensitivity	Specificity	Precision	F-Score
3	0.9371	0.8676	0.9560	0.8429	0.8551
4	0.9528	0.9412	0.9551	0.8000	0.8649
5	0.9780	0.8889	0.9962	0.9796	0.9320
6	0.9811	0.8378	1.0000	1.0000	0.9118
Average	0.9470	0.7960	0.9690	0.8060	0.7960

Fig. 5 demonstrates the performance validation of the ASRGS-OEN technique on the training dataset. The figure demonstrated that the ASRGS-OEN technique has resulted in increased performance. For instance, under class 0, the ASRGS-OEN technique has achieved an  $acc_y$  of 0.9811,  $sen_y$  of 0.7619, and  $spec_y$  of 0.9966. In line with, under class 2, the ASRGS-OEN manner has reached an  $acc_y$  of 0.9874,  $sen_y$  of 0.9756, and  $spec_y$  of 0.9892. Moreover, under class 4, the ASRGS-OEN system has attained an  $acc_y$  of 0.9654,  $sen_y$  of 0.9608, and  $spec_y$  of 0.9663. Furthermore, under class 6, the ASRGS-OEN manner has gained an  $acc_y$  of 0.9874,  $sen_y$  of 0.8919, and  $spec_y$  of 1.0000.

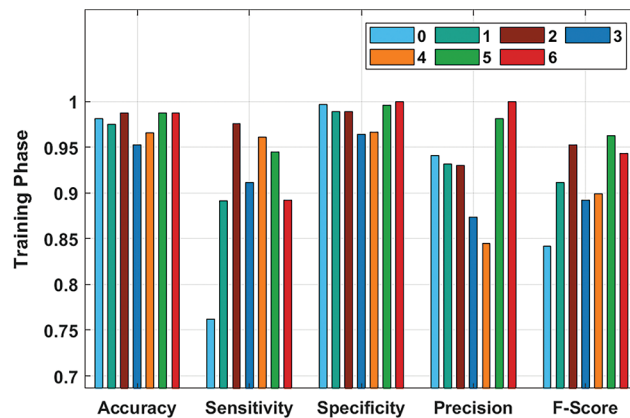
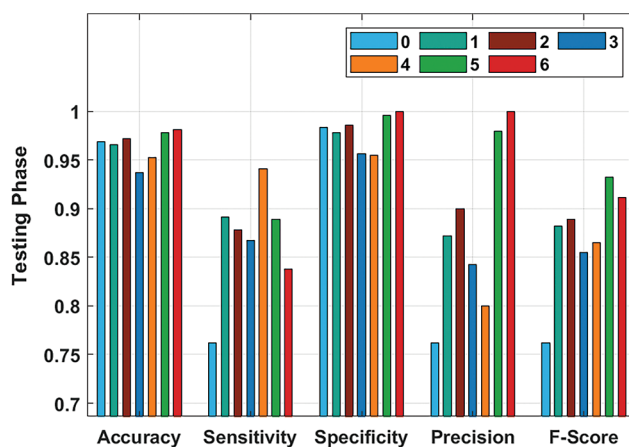
**Figure 5:** Result analysis of ASRGS-OEN model on training dataset

Fig. 6 depicts the performance validation of the ASRGS-OEN approach on the testing dataset. The figure outperformed that the ASRGS-OEN manner has resulted in higher performance. For instance, under class 0, the ASRGS-OEN manner has gained an  $acc_y$  of 0.9686,  $sen_y$  of 0.7619, and  $spec_y$  of 0.9832. Similarly, under class 2, the ASRGS-OEN approach has gained an  $acc_y$  of 0.9717,  $sen_y$  of 0.8780, and  $spec_y$  of 0.9856. Followed by, under class 4, the ASRGS-OEN approach has obtained an  $acc_y$  of 0.9528,  $sen_y$  of 0.9412, and  $spec_y$  of 0.9551. Finally, under class 6, the ASRGS-OEN methodology has gained an  $acc_y$  of 0.9811,  $sen_y$  of 0.8378, and  $spec_y$  of 1.0000.

A detailed comparative outcomes analysis of the proposed ASRGS-OEN manner with existing approaches takes place in Tab. 2 and Figs. 7, 8. On examining the performance interms of training accuracy, the ASRGS-OEN technique has gained a higher value of 0.977 whereas the VGG-16, VGG-19, MN-v1, MN-v2, R.NET-50, D-NET-201, Inception-v3, and Xception models have obtained lower values of 0.886, 0.902, 0.915, 0.924, 0.907, 0.911, 0.913, and 0.905 respectively. At the same time, on

investigative the performance with respect to testing accuracy, the ASRGS-OEN approach has attained an increased value of 0.965 whereas the VGG-16, VGG-19, MN-v1, MN-v2, R.NET-50, D-NET-201, Inception-v3, and Xception methodologies have attained minimum values of 0.849, 0.871, 0.893, 0.897, 0.879, 0.885, 0.881, and 0.875 correspondingly.



**Figure 6:** Result analysis of ASRGS-OEN model on testing dataset

**Table 2:** Results analysis of existing with proposed model on applied dataset

Methods	Training acc.	Testing acc.	Sens.	Spec.	Prec.	F-score
VGG-16	0.886	0.849	0.792	0.850	0.887	0.837
VGG-19	0.902	0.871	0.825	0.870	0.904	0.863
MN-v1	0.915	0.893	0.840	0.890	0.935	0.885
MN-v2	0.924	0.897	0.864	0.900	0.921	0.892
R.NET-50	0.907	0.879	0.812	0.880	0.931	0.868
D.NET-201	0.911	0.885	0.833	0.880	0.926	0.877
Inception-V3	0.913	0.881	0.849	0.880	0.906	0.874
Xception model	0.905	0.875	0.832	0.870	0.906	0.867
ASRGS-OEN	0.977	0.965	0.886	0.983	0.904	0.893

In addition, on scrutinizing the performance in terms of sensitivity, the ASRGS-OEN system has achieved a maximum value of 0.886 whereas the VGG-16, VGG-19, MN-v1, MN-v2, R.NET-50, D-NET-201, Inception-v3, and Xception algorithms have obtained decreased values of 0.792, 0.825, 0.840, 0.864, 0.812, 0.833, 0.849, and 0.832 correspondingly. Followed by, on inspecting the performance to specificity, the ASRGS-OEN algorithm has obtained an increased value of 0.983 whereas the VGG-16, VGG-19, MN-v1, MN-v2, R.NET-50, D-NET-201, Inception-v3, and Xception algorithms have reached minimum values of 0.850, 0.870, 0.890, 0.900, 0.880, 0.880, 0.880, and 0.870 correspondingly. Concurrently, on investigative the performance in terms of precision, the ASRGS-OEN technique has gained a superior value of 0.904 whereas the VGG-16, VGG-19, MN-v1, MN-v2, R.NET-50,

D-NET-201, Inception-v3, and Xception methods have obtained lower values of 0.887, 0.904, 0.935, 0.921, 0.931, 0.926, 0.906, and 0.906 respectively.

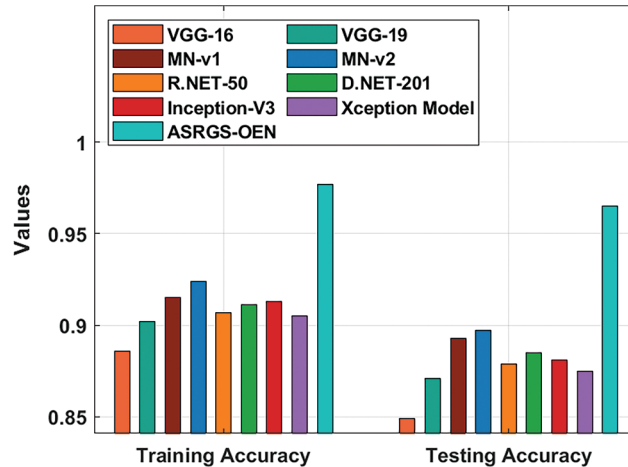


**Figure 7:** Training and testing accuracy analysis of ASRGS-OEN model

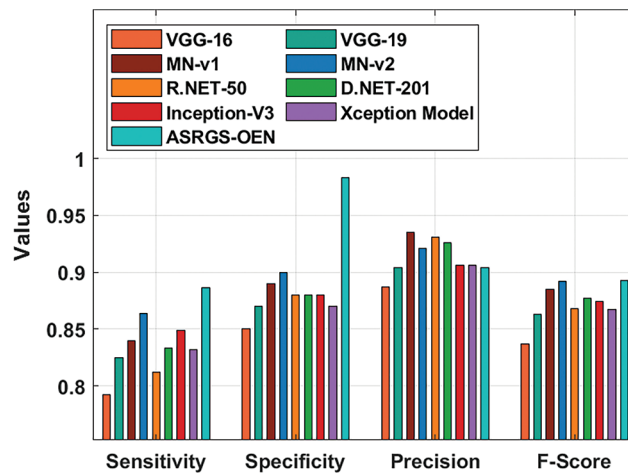


**Figure 8:** Comparative analysis of ASRGS-OEN technique with recent approaches

Lastly, on exploratory performance in terms of F-score, the ASRGS-OEN manner has gained a maximum value of 0.893 whereas the VGG-16, VGG-19, MN-v1, MN-v2, R.NET-50, D-NET-201, Inception-v3, and Xception approaches have reached reduced values of 0.837, 0.863, 0.885, 0.892, 0.868, 0.877, 0.874, and 0.867 correspondingly. By looking into the aforementioned tables and figures, it can be stated that the ASRGS-OEN approach has accomplished maximal outcomes over the other techniques under different aspects.

#### 4 Conclusion

In this study, a novel ASRGS-OEN technique is developed to diagnose and classify the different stages of skin diseases. The proposed ASRGS-OEN technique incorporates different sub-processes namely preprocessing, SRG based segmentation, EfficientNet based feature extraction, FPA based

hyper-parameter optimization, and MWAMNE based classification. Moreover, the utilization of FPA based tuning of the hyper-parameters helps to accomplish improved diagnostic outcomes. A wide-ranging simulation analysis of the ASRGS-OEN technique takes place and the results are reviewed under numerous dimensions. The training accuracy of the proposed research work is 0.977 and testing accuracy is 0.965, moreover we achieved a precision of 0.904. The simulation results highlighted the supremacy of the ASRGS-OEN technique on the applied dermoscopic images. Therefore, the ASRGS-OEN technique can be applied as a proficient tool in real-time diagnosis. In future, the ASRGS-OEN technique can be deployed in the Internet of Things (IoT) and cloud environment to assist patients from remote areas.

**Funding Statement:** The authors received no specific funding for this study.

**Conflicts of Interest:** The authors declare that they have no conflicts of interest to report regarding the present study.

## References

- [1] M. Goyal, T. Knackstedt, S. Yan and S. Hassanpour, "Artificial intelligence-based image classification for diagnosis of skin cancer: Challenges and opportunities," *Computers in Biology and Medicine*, pp. 104065, 2020.
- [2] H. W. Rogers, M. A. Weinstock, S. R. Feldman and B. M. Coldiron, "Incidence estimate of non-melanoma skin cancer (keratinocyte carcinomas) in the us population, 2012," *JAMA Dermatology*, vol. 151, no. 10, pp. 1081–1086, 2015.
- [3] F. Bray, J. Ferlay, I. Soerjomataram, R. L. Siegel, L. A. Torre et al., "Global cancer statistics 2018: GLOBOCAN estimates of incidence and mortality worldwide for 36 cancers in 185 countries," *CA: A Cancer Journal for Clinicians*, vol. 68, no. 6, pp. 394–424, 2018.
- [4] A. Hosny, C. Parmar, J. Quackenbush, L. H. Schwartz and H. J. Aerts, "Artificial intelligence in radiology," *Nature Reviews Cancer*, vol. 18, no. 8, pp. 500–510, 2018.
- [5] X. Liu, L. Faes, A. U. Kale, S. K. Wagner, D. J. Fu et al., "A comparison of deep learning performance against health-care professionals in detecting diseases from medical imaging: A systematic review and meta-analysis," *The Lancet Digital Health*, vol. 1, no. 6, pp. e271–97, 2019.
- [6] M. Havaei, A. Davy, D. W. Farley, A. Biard, A. Courville et al., "Brain tumor segmentation with deep neural networks," *Medical Image Analysis*, vol. 35, pp. 18–31, 2017.
- [7] M. Goyal, N. Reeves, S. Rajbhandari and M. H. Yap, "Robust methods for real-time diabetic foot ulcer detection and localization on mobile devices," *IEEE Journal of Biomedical and Health Informatics*, vol. 23, no. 4, pp. 1730–1741, 2018.
- [8] N. Tomita, B. Abdollahi, J. Wei, B. Ren, A. Suriawinata et al., "Attention based deep neural networks for detection of cancerous and precancerous esophagus tissue on histopathological slides," *JAMA Network Open*, vol. 2, no. 11, pp. 1914645–1914645, 2019.
- [9] S. Wang, Z. Su, L. Ying, X. Peng, S. Zhu et al., "Accelerating magnetic resonance imaging via deep learning," in *Proc. 13th Int. Symp. on Biomedical Imaging (ISBI)*, IEEE, Prague, Czech Republic, pp. 514–517, 2016.
- [10] S. Banerjee, S. K. Singh, A. Chakraborty, A. Das and R. Bag, "Melanoma diagnosis using deep learning and fuzzy logic," *Diagnostics*, vol. 10, no. 8, pp. 577–586, 2020.
- [11] M. A. Khan, M. Sharif, T. Akram, R. Damasevicius and R. Maskeliunas, "Skin lesion segmentation and multiclass classification using deep learning features and improved moth flame optimization," *Diagnostics*, vol. 11, no. 5, pp. 811, 2021.
- [12] M. Y. Sikkandar, B. A. Alrasheadi, N. B. Prakash, G. R. Hemalakshmi, A. Mohanarathinam et al., "Deep learning based an automated skin lesion segmentation and intelligent classification model," *Journal of Ambient Intelligence and Humanized Computing*, vol. 12, no. 3, pp. 3245–3255, 2021.
- [13] P. N. Srinivasu, J. G. SivaSai, M. F. Ijaz, A. K. Bhoi, W. Kim et al., "Classification of skin disease using deep learning neural networks with MobileNet V2 and LSTM," *Sensors*, vol. 21, no. 8, pp. 2852–2906, 2021.

- [14] T. Lee, V. Ng, R. Gallagher, A. Coldman and D. McLean, "Dullrazor: A software approach to hair removal from images," *Computers in Biology and Medicine*, vol. 27, no. 6, pp. 533–543, 1997.
- [15] N. Shrivastava and J. Bharti, "Automatic seeded region growing image segmentation for medical image segmentation: A brief review," *International Journal of Image and Graphics*, vol. 20, no. 3, pp. 2050018–2050034, 2020.
- [16] P. Zhang, L. Yang and D. Li, "EfficientNet-B4-ranger: A novel method for greenhouse cucumber disease recognition under natural complex environment," *Computers and Electronics in Agriculture*, vol. 176, pp. 105652–105674, 2020.
- [17] M. Azad, O. B. Haddad and X. Chu, "Flower pollination algorithm (FPA)," in *Proc. of Advanced Optimization by Nature-Inspired Algorithms*, Springer, Singapore, pp. 59–67, 2018.
- [18] F. An, X. Li and X. Ma, "Medical image classification algorithm based on visual attention mechanism-MCNN," *Oxidative Medicine and Cellular Longevity*, vol. 2021, no. 6280690, pp. 1–12, 2021.
- [19] C. F. Codella, D. Gutman, M. C. Emre, H. Brian, A. Michael *et al.*, "Skin lesion analysis toward melanoma detection: A challenge at the 2017 international symposium on biomedical imaging (isbi), hosted by the international skin imaging collaboration (isic)," in *The Proc. IEEE 15th Int. Symp. on Biomedical Imaging (ISBI 2018)*, DC, USA, pp. 168–172, 2018.